Обзор ArXiv:astro-ph, 13-17 ноября 2017 года

От Сильченко О.К.

Astro-ph: 1711.04314

NEARBY EARLY-TYPE GALACTIC NUCLEI AT HIGH RESOLUTION – DYNAMICAL BLACK HOLE AND NUCLEAR STAR CLUSTER MASS MEASUREMENTS

Dieu D. Nguyen[1], Anil C. Seth[1], Nadine Neumayer[2], Sebastian Kamann[3], Karina T. Voggel[1], Michele Cappellari[4], Arianna Picotti[2], Phuong M. Nguyen[5], Torsten Böeker[6], Victor Debattista[7], Nelson Caldwell[8], Richard McDermid[9], and Bastian Nathan[3]

Draft version November 15, 2017

ABSTRACT

We present a detailed study of the nuclear star clusters (NSCs) and massive black holes (BHs) of four of the nearest low-mass early-type galaxies: M32, NGC205, NGC5012, and NGC5206. We measure dynamical masses of both the BHs and NSCs in these galaxies using Gemini/NIFS or VLT/SINFONI stellar kinematics, *Hubble Space Telescope* (*HST*) imaging, and Jeans Anisotropic Models. We detect massive BHs in M32, NGC5102, and NGC5206, while in NGC205, we find only an upper limit. These BH mass estimates are consistent with previous measurements in M32 and NGC205, while those in NGC5102 & NGC5206 are estimated for the first time, and both found to be $<10^6$ $M_\odot$. This adds to just a handful of galaxies with dynamically measured sub-million $M_\odot$ central BHs. Combining these BH detections with our recent work on NGC404's BH, we find that 80% (4/5) of nearby, low-mass ($10^9 - 10^{10} M_\odot$; $\sigma_\star \sim 20 - 70$ km s^{-1}) early-type galaxies host BHs. Such a high occupation fraction suggests the BH seeds formed in the early epoch of cosmic assembly likely resulted in abundant seeds, favoring a low-mass seed mechanism of the remnants, most likely from the first generation of massive stars. We find dynamical masses of the NSCs ranging from $2 - 80 \times 10^6 M_\odot$ and compare these masses to scaling relations for NSCs based primarily on photometric mass estimates. Color gradients suggest younger stellar populations lie at the centers of the NSCs in three of the four galaxies (NGC205, NGC5102, and NGC5206), while the morphology of two are complex and are best-fit with multiple morphological components (NGC5102 and NGC5206). The NSC kinematics show they are rotating, especially in M32 and NGC5102 ($V/\sigma_\star \sim 0.7$).

Объекты

TABLE 4
HOST GALAXIES PROPERTIES

	M32	NGC205	NGC5102	NGC5206
Distance (Mpc)	0.79 [1]	0.82 [2]	3.2 [3]	3.5 [4]
$m - M$ (mag)	24.49	24.75	27.52	27.72
Scale (pc/″)	4.0	4.3	16.0	17.0
$M_{B,0}$, $M_{V,0}$, $M_{I,0}$ (mag)	−16.3 [5], ..., −16.7 [6]	−15.0 [7],..., −16.5 [7]	−16.5 [5], ..., ...,	−16.2 [5], ..., ...
Total Stellar Mass ($M_\odot$)	1.0×10^9 [8, ⋆]	1.0×10^9 [11]/1.1×10^9 [⋆]	7.0×10^9 [9]/6.8×10^9 [⋆]	2.8×10^9 [CGS]/2.6×10^9 [⋆]
Effective Radius ($r_{\rm eff.}^{\rm galaxy}$)	30″/120 pc [10, ⋆]	121″/520 pc [11, ⋆]	75″/1200 pc [12, 13, ⋆]	58″/986 pc [⋆]
$\sigma_\star$ (peak/average) (km s^{-1})	120/80 [6]	21/18 [14]	58.4/42.3 [15, ⋆]	45.3/35.4 [⋆]
$v_{\rm sys.}^{\rm NED}$ or $v_{\rm sys.}^{\rm Measured}$ (km s^{-1})	−200/−201	−241/−241	+473/+472	+571/+573
Position Angle$^{\rm NED}$ (°)	45.5	170.0	48.0	45.0
Inclination (°)	70.0 [16]	...	86.0 [16]	...

NOTE. — The subscripts $_{B,V,I}$ indicate the measurements in $B-$, $V-$, and $I-$band. NED: NASA/IPAC Extragalactic Database. [CGS]: indicates the Carnegie-Irvine Galaxy Survey color profiles for total stellar masses assuming Bell & de Jong (2001) color–M/L relation. References – [1]: Welch et al. (1986); [2]: McConnachie et al. (2005); [3]: van den Bergh (1976); [4]: Tully et al. (2015); [5]: http://leda.univ-lyon1.fr/search.html; [6]: Seth (2010); [7]: Geha et al. (2006); [8]: Richstone & Sargent (1972); [9]: Davidge (2015); [10]: Graham (2002); [11]: De Rijcke et al. (2006); [12]: Jarrett et al. (2003, LGA); [13]: Davidge (2008); [14]: Valluri et al. (2005); [15]: Mitzkus et al. (2017); [16]: Verolme et al. (2002); [⋆]: this work estimates. To calculate properties from multiple references, we take their mean.

Спектральные наблюдения

TABLE 2
GEMINI/NIFS AND VLT/SINFONI SPECTROSCOPIC DATA

Object	Observation	UT Date	Instrument	Exptime (s)	Sky	Pixel Scale ($''$/pix)	$\overline{\text{FWHM}}$ (Å)	$\overline{\text{FWHM}}$ (km s^{-1})	PID
(1)	(2)	(3)	(4)	(5)	(6)	(7)	(8)	(9)	(10)
M32	NIFS	2005 Oct 23	AO + NGS	6×600	5×600	0.05	4.2	57.0	GN-2005B-SV-121
NGC205	NIFS	2008 Sep 19	AO + LGS	8×760	6×760	0.05	4.2	55.7	GN-2008B-Q-74
NGC5102	SINFONI	2007 Mar 21	UT4-Yepun	12×600	12×600	0.05	6.2	82.2	078.B-0103(A)
NGC5206	SINFONI	2011 Apr 28	UT4-Yepun	3×600	3×600	0.05	6.2	82.2	086.B-0651(B)
NGC5206	SINFONI	2013 Jun 18	UT4-Yepun	3×600	3×600	0.05	6.2	82.2	091.B-0685(A)
NGC5206	SINFONI	2014 Mar 22	UT4-Yepun	3×600	3×600	0.05	6.2	82.2	091.B-0685(A)

NOTE. — Column 1: galaxy name. Column 2: name of observations in which the data were taken. Column 3: the Universal Time date when the observations were processing. Column 4: the instrumentation in which the data were taken. Column 5: the exposure times of the observations. Column 6: the sky-off sources exposures during the observations. Column 7: the pixel scale of each camera. Columns 8 and 9: the median FWHM for the galactic nuclei cubes at ($R \sim 5500$ Å), which is used to create the line spread function used in pPXF stellar kinematics. Column 10: the principle investigator identification numbers.

Фотометрия

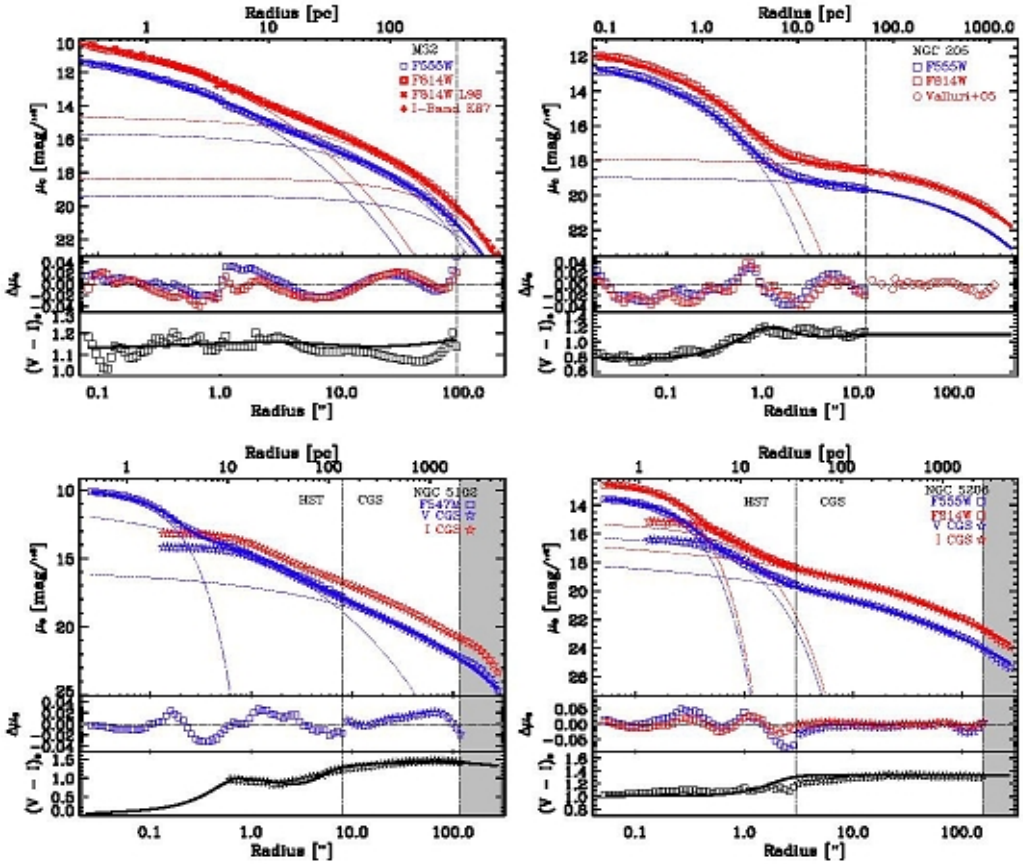

FIG. 1.— The surface brightness profiles of each galaxy studied here. The profiles are constructed from a combination of ground-based and *HST* imaging. The blue lines show V/F555W/F547M profiles, while the red lines show I/F814W profiles. All magnitudes/colors are corrected for foreground extinction. Symbols show the data, while the best fitting 1D surface brightness profiles are shown as solid lines. Each component of the best-fit models are also plotted for visualization (the innermost Sérsic component is shown in dotted line, the second largest is shown as a dashed, and when present, the outermost component is shown in the long-dashed line). The residuals of the fits are shown in the middle-panel plots and the $(V-I)_o$ color profiles are illustrated in the bottom-panel plots including the data (open-black symbols) and the best-fit model (black solid line). Different symbols are plotted correspondingly to their data set, which are shown in the legend of each top panel. The inner and outer vertical dashed lines show the ends of the *HST* and ground-based data, respectively. The grey regions in the plots of NGC5102 and NGC5206 indicate the areas beyond our fitting radius.

Фотометрия

Object	Filter	SB	n_i	$r_{\rm eff.,}i$ ($''$)	$r_{\rm eff.,}i$ (pc)	m_i (mag)	PA$_i$ (°)	b/a$_i$	$\chi^2_{\rm r}$	$L_{\star,i}$ ($\times10^7 L_\odot$)	$M_{\star,i,\ \rm pop.}$ ($\times10^7 M_\odot$)	Comp.
(1)	(2)	(3)	(4)	(5)	(6)	(7)	(8)	(9)	(10)	(11)	(12)	(13)
							Free PA					
M32	F814W	2D	2.7±0.3	1.1±0.1	4.4±0.4	11.0±0.1	−23.4±0.5	0.75±0.03		1.0±0.1	1.45±0.15	NSC
		2D	1.6±0.1	27.0±1.0	108±4	7.0±0.1	−24.7±0.4	0.79±0.07	1.7	44.7±0.7	82.4±1.7	Bulge
		1D*	1	129	516	8.6	−25.0±0.7	0.79±0.05		9.5±0.5	20.3±0.7	Disk
							Fixed PA					
M32	F814W	2D	2.7±0.3	1.1±0.1	4.4±0.4	11.1±0.1	−25.0	0.75±0.09		1.0±0.1	1.50±0.20	NSC
		2D	1.6±0.1	27.0±1.0	108±4	7.1±0.1	−25.0	0.79±0.11	2.0	44.0±0.7	81.0±1.5	Bulge
		1D*	1	129	516	8.6	−25.0	0.79±0.08		9.5±0.5	20.3±0.7	Disk
							Free PA					
NGC205	F814W	2D	1.6±0.2	0.3±0.1	1.3±0.2	14.0±0.2	−37.1±1.4	0.95±0.03		0.10±0.07	0.2±0.1	NSC
		1D*	1.4	120	516	7.0	−40.4±1.0	0.90±0.07	5.5	54.0±7.0	108±13	Bulge
							Fixed PA					
NGC205	F814W	2D	1.6±0.2	0.3±0.1	1.3±0.2	14.0±0.2	−40.4	0.95±0.06		0.10±0.05	0.2±0.1	NSC
		1D*	1.4	120	516	7.0	−40.4	0.91±0.05	5.9	54.0±7.0	108±10	Bulge
							Free PA					
NGC5102	F547M	2D	0.8±0.2	0.1±0.1	1.6±1.6	15.5±0.4	55.1±1.5	0.68±0.06		1.8±0.4	1.1±0.2	NSC$_1$
		2D	3.1±0.1	2.0±0.3	32.0±4.8	13.8±0.3	51.1±1.7	0.59±0.04	3.3	8.5±0.5	6.80±0.3	NSC$_2$
		1D*	3	75	1200	9.3	50.0	0.60±0.07		210±8	674±10	Bulge
							Fixed PA					
NGC5102	F547M	2D	0.8±0.2	0.1±0.1	1.6±1.6	15.5±0.4	50.5	0.68±0.05		1.8±0.4	1.1±0.2	NSC$_1$
		2D	3.1±0.1	2.0±0.3	32.0±4.8	13.8±0.3	50.5	0.60±0.08	3.6	8.5±0.5	6.80±0.3	NSC$_2$
		1D*	3	75	1200	10.1	50.5	0.63±0.10		210±8	674±18	Bulge
							Free PA					
NGC5206	F814W	2D	0.8±0.1	0.2±0.1	3.4±1.7	16.7±0.3	36.0±0.1	0.96±0.03		0.09±0.03	0.17±0.04	NSC$_1$
		2D	2.3±0.3	0.6±0.1	10.5±1.7	14.8±0.2	38.5±1.4	0.96±0.02	2.4	0.64±0.05	1.28±0.07	NSC$_2$
		1D*	2.57	58	986	10.1	38.6	0.98±0.01		122±5	260±12	Bulge
							Fixed PA					
NGC5206	F814W	2D	0.8±0.1	0.2±0.1	3.4±1.7	16.7±0.3	38.3	0.96±0.03		0.09±0.03	0.17±0.04	NSC$_1$
		2D	2.3±0.3	0.6±0.1	10.2±1.7	14.8±0.2	38.3	0.97±0.03	2.7	0.64±0.05	1.28±0.07	NSC$_2$
		1D*	2.57	58	986	9.1	38.3	0.98±0.01		122±5	260±12	Bulge

NOTE — Column 1: galaxy name. Columns 2: the filters in which the images were observed. Column 3: the Sérsic

Кинематика

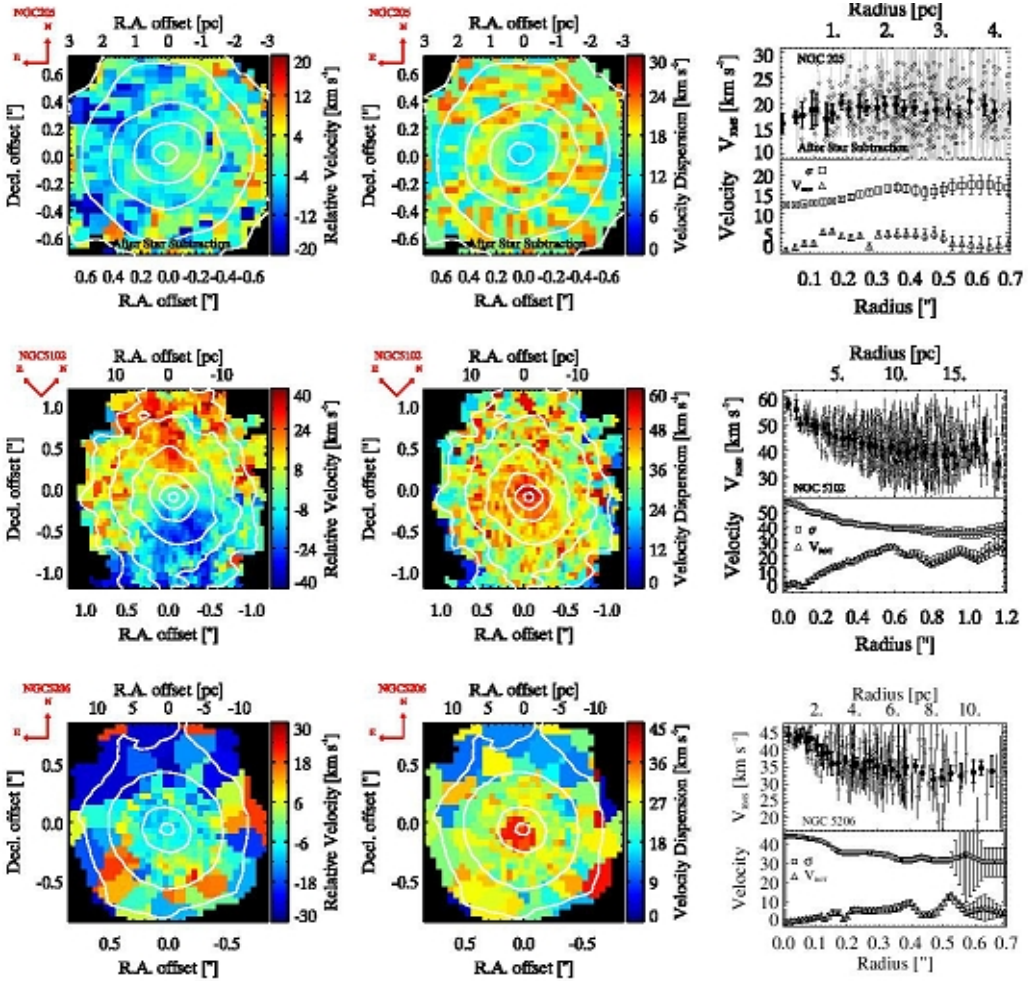

FIG. 5.— Stellar kinematic maps derived from CO bandhead spectroscopy from Gemini/NIFS (NGC205) and VLT/SINFONI (NGC5102 and NGC5206) spectroscopic data. Radial velocity maps are shown in the left column, and dispersion maps in the middle column. The radial velocity is shown relative to the systemic velocity of -241 ± 2 km s^{-1}(NGC205), 472 ± 2 km s^{-1}(NGC5102), 573 ± 5 km s^{-1}(NGC5206). The top plots show the NGC205 stellar kinematics after removing individual bright stars (Section 5.2). White contours show the stellar continuum; and the red arrows indicate the orientation. Kinematics are only plotted out to the radii where they are reliable; black pixels indicate data not used in the JAM modeling. In the right plots, the top-panel shows the $V_{\rm RMS} = \sqrt{V^2 + \sigma^2}$ (open diamonds), with the filled black dots showing the bi-weighted $V_{\rm RMS}$ in the circular annuli. The error bars are 1σ deviations of the kinematic measurements of the Voronoi bins in the same annuli. The KINEMETRY decomposition (Krajnović et al. 2006) of dispersion (open squares) and rotation (open triangles) curves are shown in the bottom-panel.

Ограничение на параметры

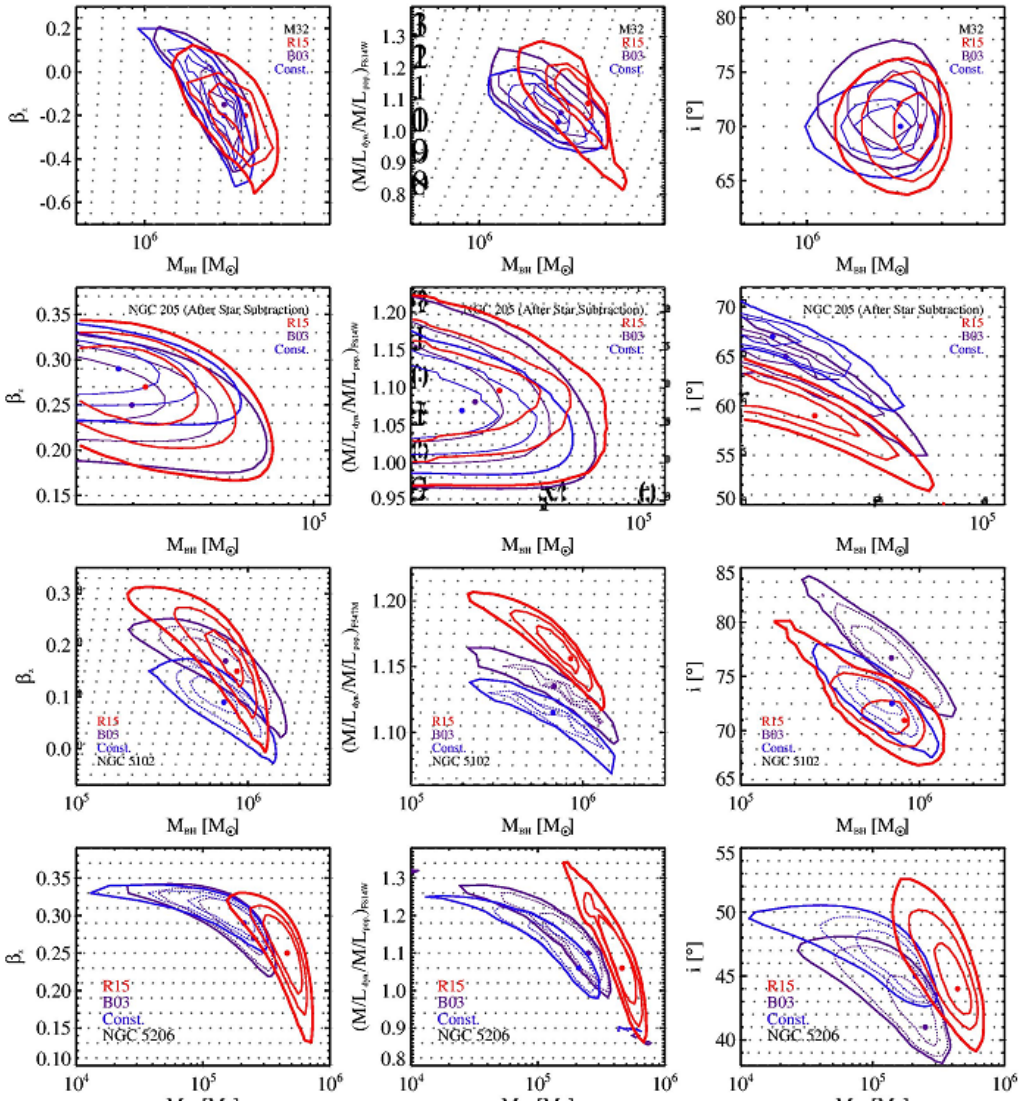

Описание профилей скорости – с черной дырой и без

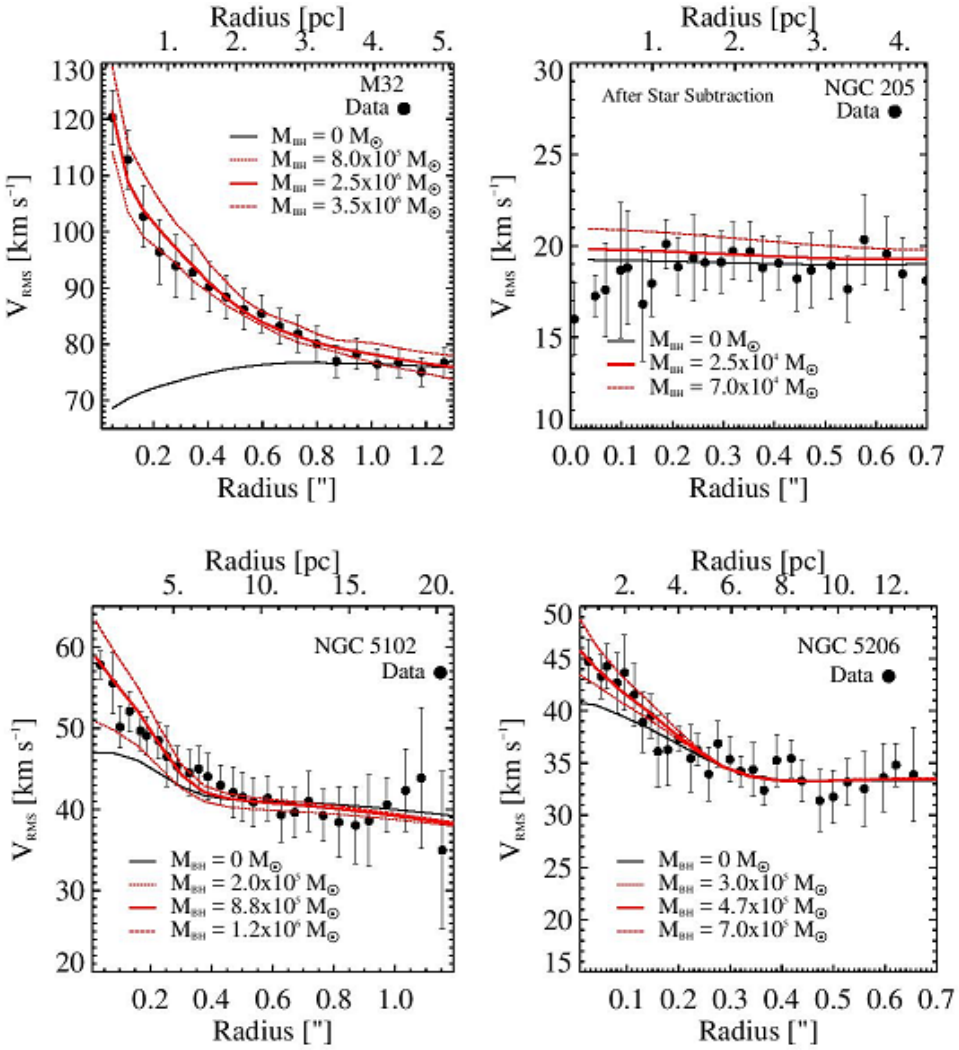

FIG. 7.— 1D V_{RMS} vs. JAM predictions of mass models with varying BH masses. The red solid lines show our best-fit JAM models. Long-dashed and short-dashed lines indicate the upper and lower range of BH masses within 3σ (see Figure 6 and Table 6), while the black line shows the best-fit JAM models without a BH. All models are fixed to the corresponding best-fit inclination angles of galaxies (column 9, Table 6) but varying for anisotropy, mass scaling ratio,

Про массы черных дыр в карликах

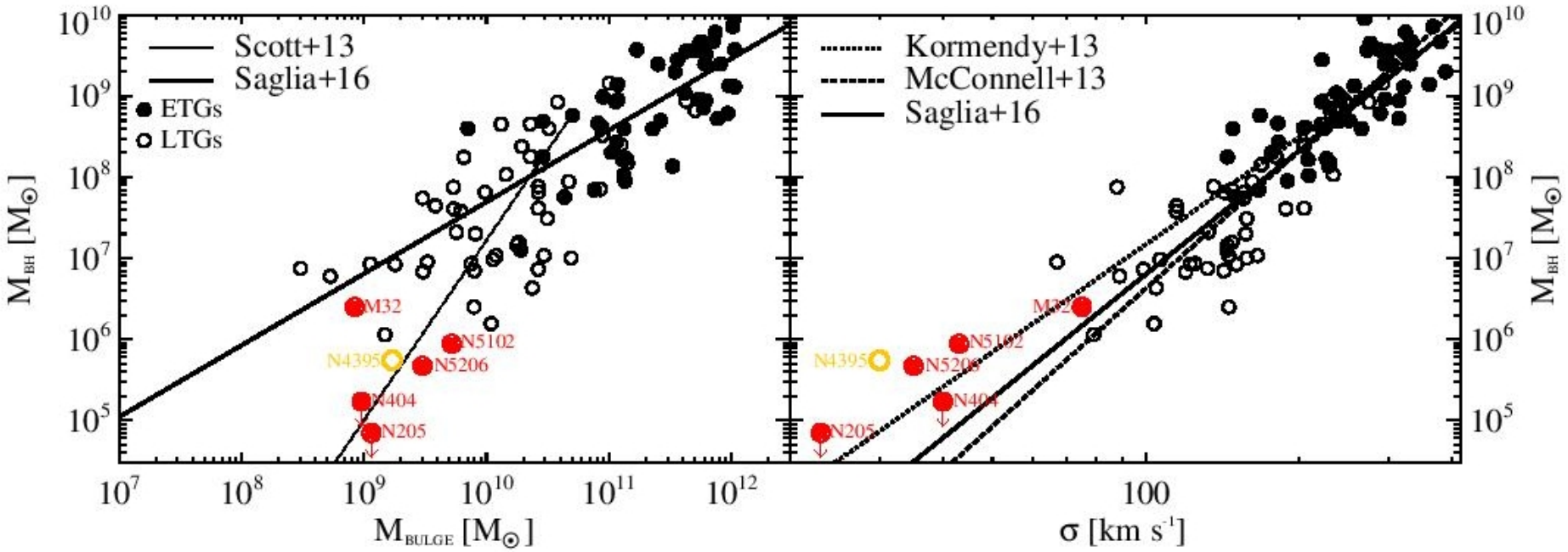

FIG. 10.— Our four low-mass early-type galaxies in context of the M_{BH}–M_{Bulge} (left) and M_{BH}–σ (right) scaling relations. The data of both early-type galaxies (ETGs, black dots with open circles) and late-type galaxies (black open circles) are taken from the compilation of Saglia et al. (2016). The dotted-, dashed-, long dashed-, and solid-lines indicate their linear best-fit in log scale of the relations from Scott et al. (2013); McConnell & Ma (2013); Kormendy & Ho (2013), and Saglia et al. (2016) for early-type galaxies (LTGs), respectively. The BH masses of M32, NGC5102, and NGC5206 and 3σ upper limit mass of NGC205 with the downward arrow are plotted in red dots + open circles as in the legend. We also add BHs with dynamical masses below $10^6 M_\odot$, including the dwarf AGN late-type galaxy NGC4395 (yellow open circle; den Brok et al. 2015) and early-type galaxy NGC404 (Nguyen et al. 2017).

Про центральное скопление

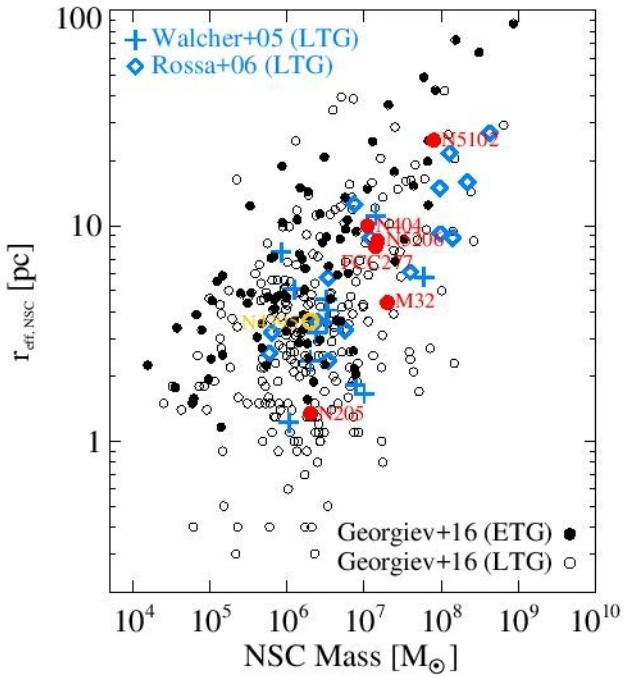

FIG. 9.— Mass vs. size for NSCs. Our dynamical mass determinations plus that of NGC404 Nguyen et al. (2017) are shown in red (dots + outer circles); these are the only dynamically determined NSC masses in early-type galaxies (ETGs). These are compared to photometric estimates from Georgiev et al. (2016) plotted both in black circles with central dots for ETGs and in black open

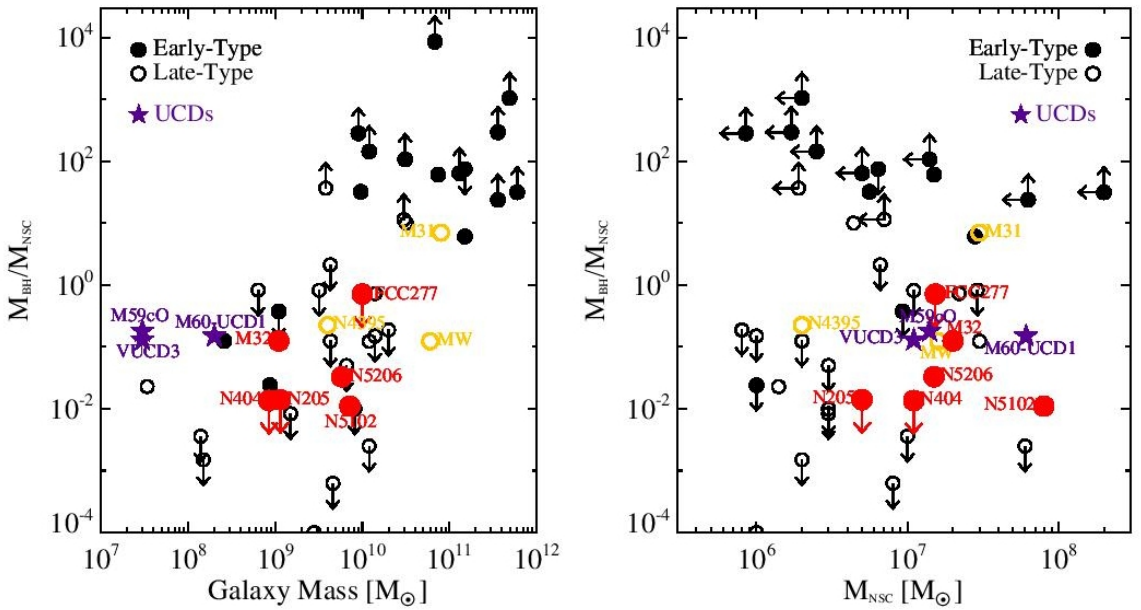

FIG. 12.— Ratio of the BH and NSC mass against their host-galaxy stellar mass (left) and their NSC dynamical masses based on dynamical measurements of $M/L_{\rm dyn.}$ (right). Original data with dynamical measurements are shown with early- (black dots), late-type (gray dots) galaxies, and current BH mass measurements of UCDs (black stars) are taken from Neumayer & Walcher (2012), Graham & Spitler (2009), Lyubenova et al. (FCC277; 2013), Seth et al.

Astro-ph: 1711.05272

THE STELLAR POPULATIONS OF TWO ULTRA-DIFFUSE GALAXIES FROM OPTICAL AND NEAR-INFRARED PHOTOMETRY

VIRAJ PANDYA[1], AARON J. ROMANOWSKY[2,3], SEPPO LAINE[4], JEAN P. BRODIE[1,3], BENJAMIN D. JOHNSON[5], WILLIAM GLACCUM[4], JEAN-CHARLES CUILLANDRE[6], STEPHEN GWYN[7], JESSICA KRICK[4], RONALD LASKER[8], IGNACIO MARTÍN-NAVARRO[1,3], DAVID MARTINEZ-DELGADO[9], PIETER VAN DOKKUM[10], ALEXA VILLAUME[1]

[1]Department of Astronomy and Astrophysics, University of California, Santa Cruz, CA 95064, USA
[2]Department of Physics & Astronomy, San Josè State University, One Washington Square, San Jose, CA 95192, USA
[3]University of California Observatories, 1156 High Street, Santa Cruz, CA 95064, USA
[4]IPAC, Mail Code 314-6, Caltech, 1200 E. California Blvd., Pasadena, CA 91125, USA
[5]Harvard-Smithsonian Center for Astrophysics, 60 Garden St., Cambridge, MA 02138, USA
[6]CEA/IRFU/SAp, Laboratoire AIM Paris-Saclay, CNRS/INSU, Universit Paris Diderot, Observatoire de Paris, PSL Research University, F-91191 Gif-sur-Yvette Cedex, France
[7]Herzberg Institute of Astrophysics, National Research Council of Canada, Victoria, BC V9E 2E7, Canada
[8]Finnish Centre for Astronomy with ESO (FINCA), University of Turku, Väisäläntie 20, FI-21500 Kaarina, Finland
[9]Astronomisches Rechen-Institut, Zentrum für Astronomie, Universität Heidelberg, Mönchhofstr. 12–14, 69120 Heidelberg, Germany
and
[10]Astronomy Department, Yale University, New Haven, CT 06511, USA

(Dated: November 16, 2017)
Draft version November 16, 2017

ABSTRACT

We present observational constraints on the stellar populations of two ultra-diffuse galaxies (UDGs) using optical through near-infrared (NIR) spectral energy distribution (SED) fitting. Our analysis is enabled by new *Spitzer*-IRAC 3.6 μm and 4.5 μm imaging, archival optical imaging, and the `prospector` fully Bayesian SED fitting framework. Our sample contains one field UDG (DGSAT I), one Virgo cluster UDG (VCC 1287), and one Virgo cluster dwarf elliptical for comparison (VCC 1122). Independently of SED fitting, we find that the optical–NIR colors of the three galaxies are significantly different from each other. We infer that VCC 1287 has an old ($\gtrsim 7.7$ Gyr) and surprisingly metal-poor ($[Z/Z_{\odot}] \lesssim -1.0$) stellar population, even after marginalizing over uncertainties on diffuse interstellar dust. In contrast, the field UDG DGSAT I shows evidence of being younger than the Virgo UDG, with an extended star formation history and an age posterior extending down to ~ 3 Gyr. The stellar

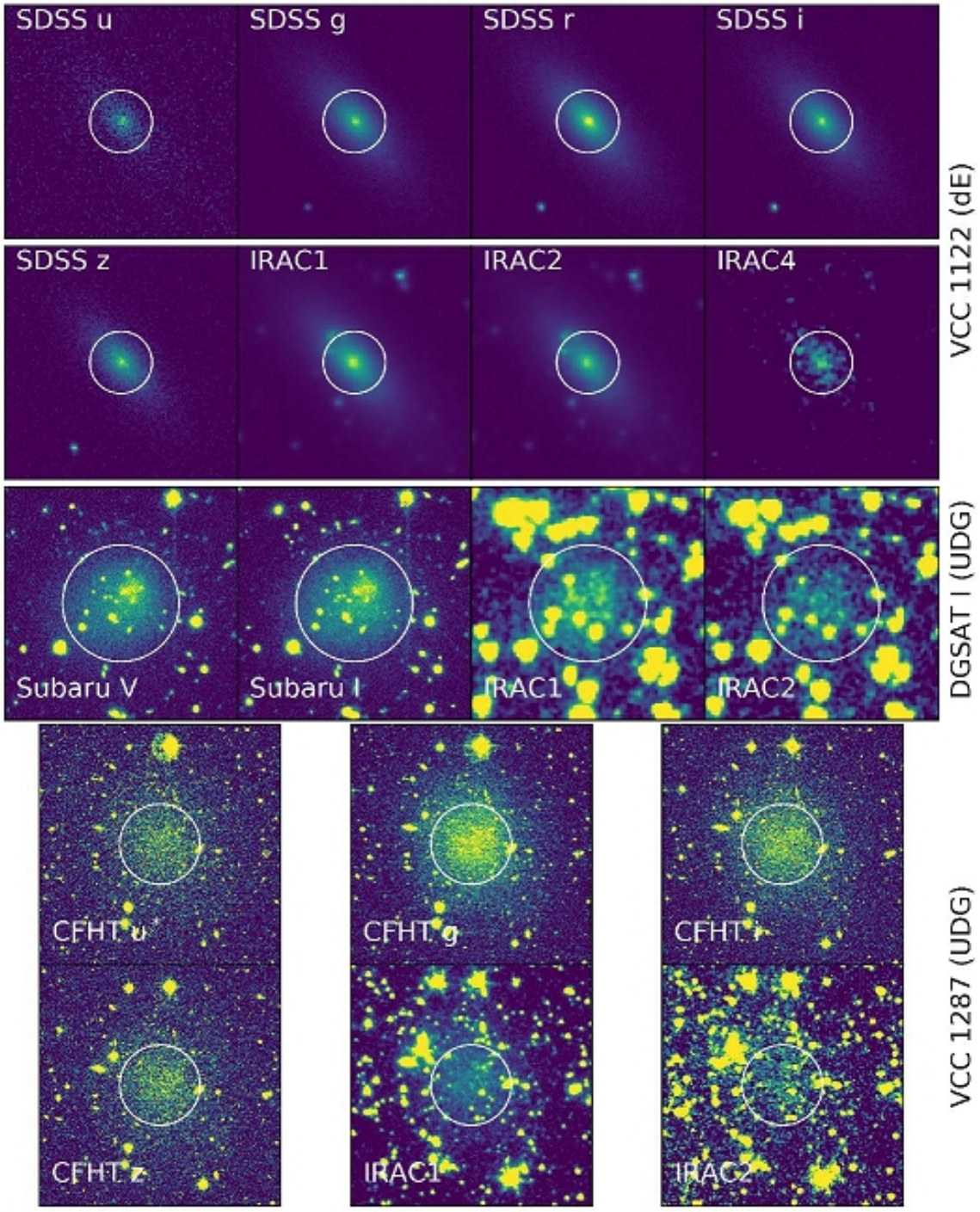
SDSS u
SDSS g
SDSS r
SDSS i
SDSS z
IRAC1
IRAC2
IRAC4
VCC 1122 (dE)
Subaru V
Subaru I
IRAC1
IRAC2
DGSAT I (UDG)
CFHT u
CFHT g
CFHT r
CFHT z
IRAC1
IRAC2
VCC 1287 (UDG)

Модели звездных населений по SED

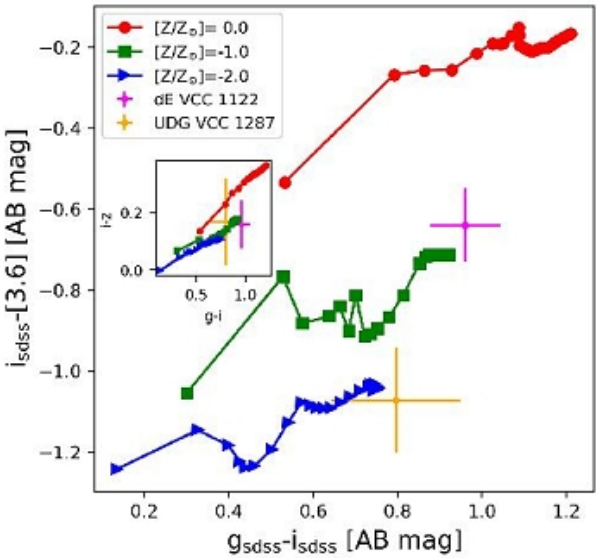

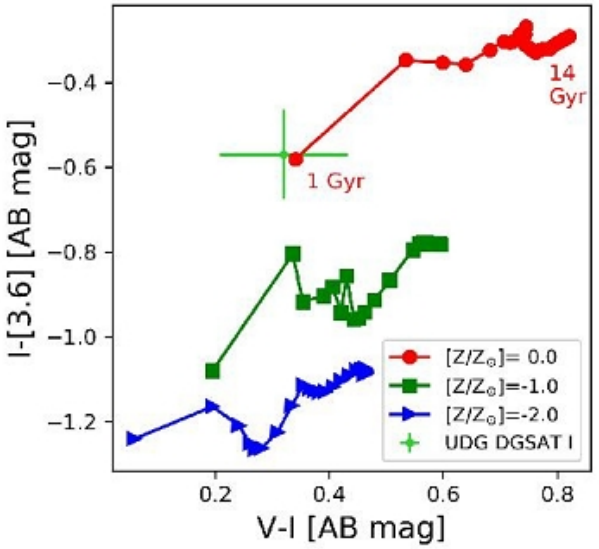

Table 5
`prospector` Results With Dust

Parameter	VCC 1122	DGSAT I	VCC 1287
$\log M_*/M_\odot$	$7.83^{+0.06}_{-0.09}$	$8.12^{+0.16}_{-0.18}$	$7.82^{+0.05}_{-0.10}$
$[Z/Z_\odot]$	$-1.05^{+0.31}_{-0.73}$	$-0.63^{+0.35}_{-0.62}$	< -1.55
τ [Gyr]	< 1.81	> 3.20	< 1.93
$t_{\rm age}$ [Gyr]	> 7.56	$6.81^{+4.08}_{-3.02}$	> 8.66
A_V [mag]	< 0.42	< 0.26	< 0.16

Note. — Summary statistics for the marginalized posterior of each free parameter shown in Figure 4, in the case where diffuse interstellar dust is fit as a free parameter with a uniform prior of $A_V = 0-4$ mag. In cases where the posterior distribution is skewed and hitting up against the prior limit (e.g., $t_{\rm age} = 14$ Gyr), we instead give either the lower or upper limit (16th or 84th percentile, respectively). Otherwise, the 16th, 50th and 84th percentiles of the posterior distribution are given. Note that the stellar masses given here are aperture masses; total stellar masses derived via GALFIT are given in subsection 3.6.

Table 6
`prospector` Results With Minimal/No Dust

Parameter	VCC 1122	DGSAT I	VCC 1287
$\log M_*/M_\odot$	$7.84^{+0.05}_{-0.06}$	$8.13^{+0.14}_{-0.14}$	$7.80^{+0.07}_{-0.11}$
$[Z/Z_\odot]$	$-0.70^{+0.13}_{-0.16}$	$-0.27^{+0.25}_{-0.22}$	$-1.56^{+0.52}_{-0.19}$
τ [Gyr]	< 1.77	> 3.21	< 2.12
$t_{\rm age}$ [Gyr]	> 8.59	$7.12^{+3.79}_{-2.79}$	> 7.74
A_V [mag]	$0.010^{+0.007}_{-0.006}$	–	–

Note. — Same as Table 5 but now we assume zero diffuse interstellar dust (A_V fixed to 0 mag) for the two UDGs. For the dE, instead of fixing $A_V = 0$ mag, we include IRAC4 in the fit and assume a uniform prior over $A_V = 0 - 4$ mag. The vastly reduced confidence interval for A_V shows that IRAC4 alone is quite helpful

В рамках общей зависимости масса-металличность

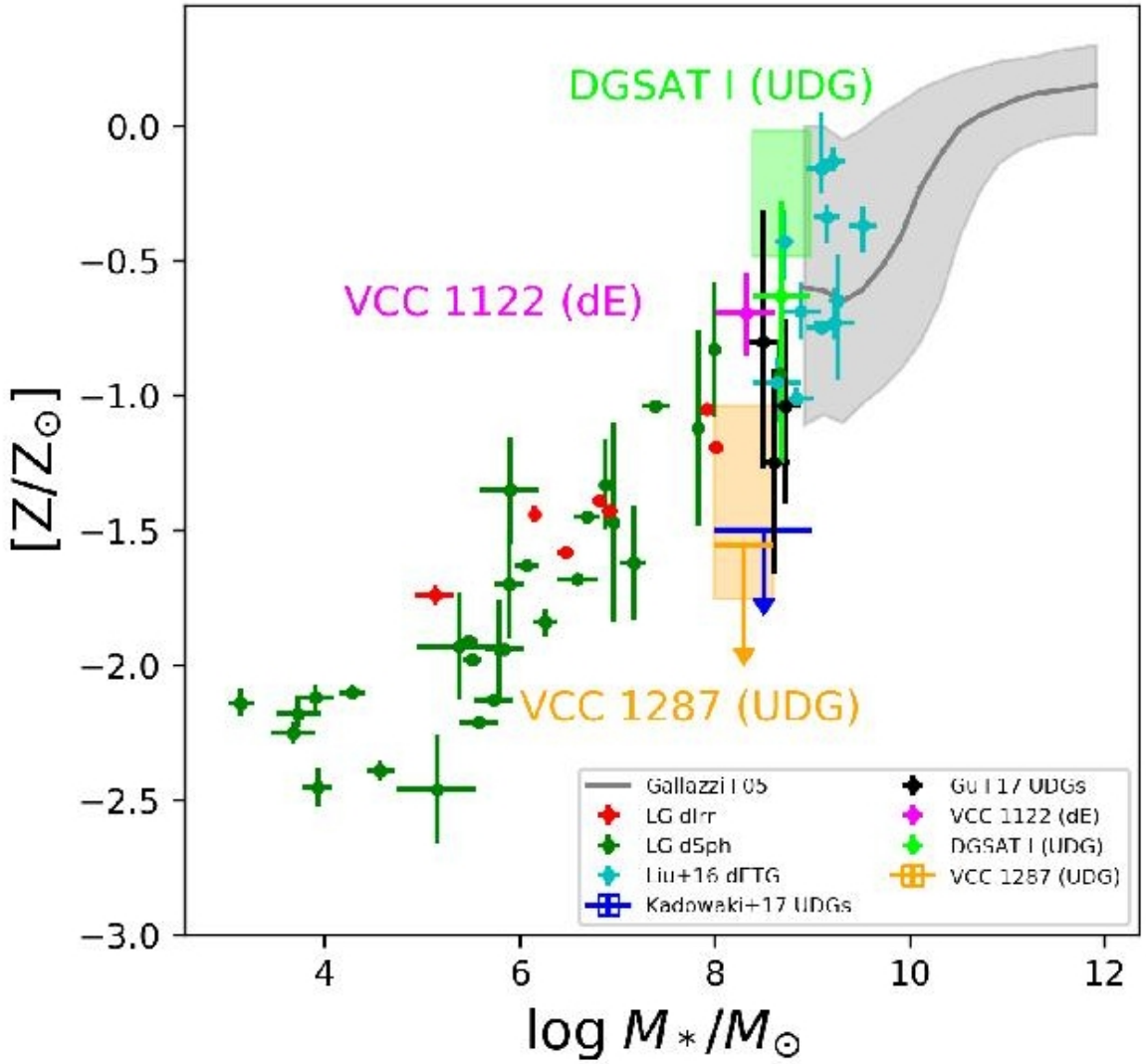

Astro-ph:1711.05813

Galaxy structure from multiple tracers: III. Radial variations in M87's IMF

Lindsay Oldham[1⋆†] & Matthew Auger[2]
[1] *Harvard-Smithsonian Center for Astrophysics, 60 Garden Street, Cambridge, MA 02138, USA*
[2] *Institute of Astronomy, University of Cambridge, Madingley Road, Cambridge CB3 0HA, UK*

November 17, 2017

ABSTRACT
We present the first constraints on stellar mass-to-light ratio gradients in an early-type galaxy (ETG) using multiple dynamical tracer populations to model the dark and luminous mass structure simultaneously. We combine the kinematics of the central starlight, two globular cluster populations and satellite galaxies in a Jeans analysis to obtain new constraints on M87's mass structure, employing a flexible mass model which allows for radial gradients in the stellar mass-to-light ratio. We find that, in the context of our model, a radially declining stellar-mass-to-light ratio is strongly favoured. Modelling the stellar mass-to-light ratio as following a power law, $\Upsilon_\star \sim R^{-\mu}$, we infer a power-law slope $\mu = -0.54 \pm 0.05$; equally, parameterising the stellar-mass-to-light ratio via a central mismatch parameter relative to a Salpeter IMF, α, and scale radius R_M, we find $\alpha > 1.48$ at 95% confidence and $R_M = 0.35 \pm 0.04$ kpc. We use

Анализ захватывает как область доминирования звезд, так и область доминирования темной материи

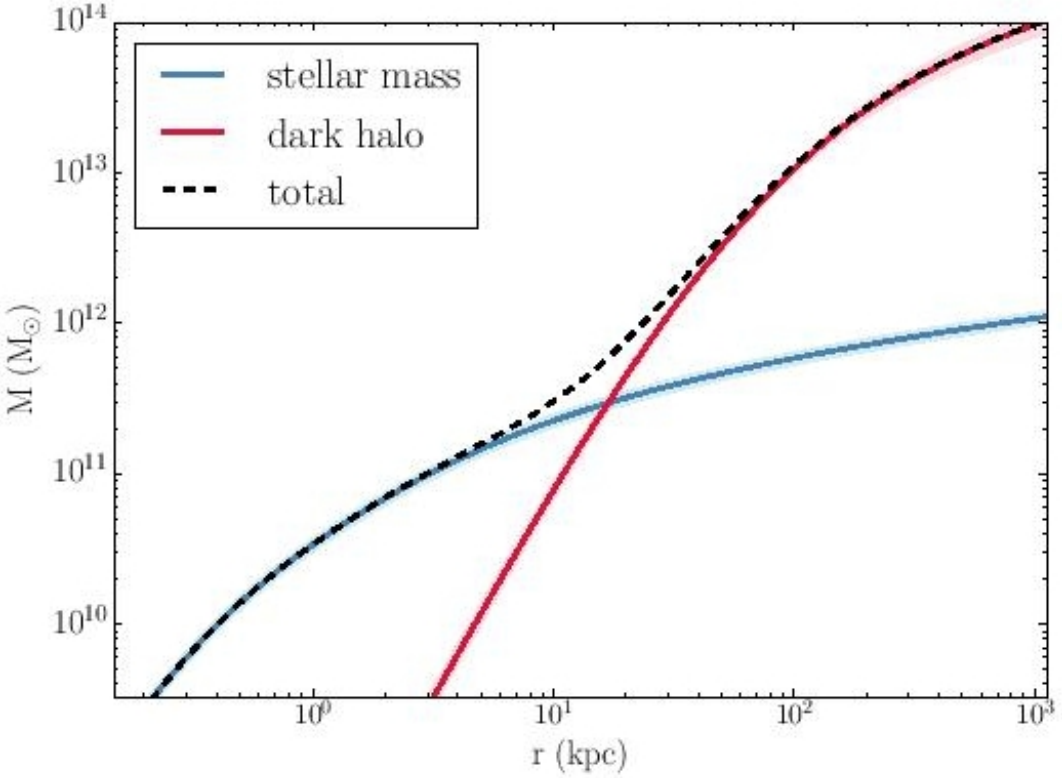

Figure 2. Inference on the dark, stellar and total mass profile in the anisotropic model. At radii $\leqslant$ 10 kpc $\sim R_e$, the stellar mass dominates, whereas beyond this, the dark halo becomes the main contributor to the potential. Our kinematic data extend from $\sim$ 10 pc to 1 Mpc, which is the radius range spanned in this Figure. Note that we include systematic uncertainties as described in Section 5.

Отпустили отношение плотность-яркость «на волю», и вот…

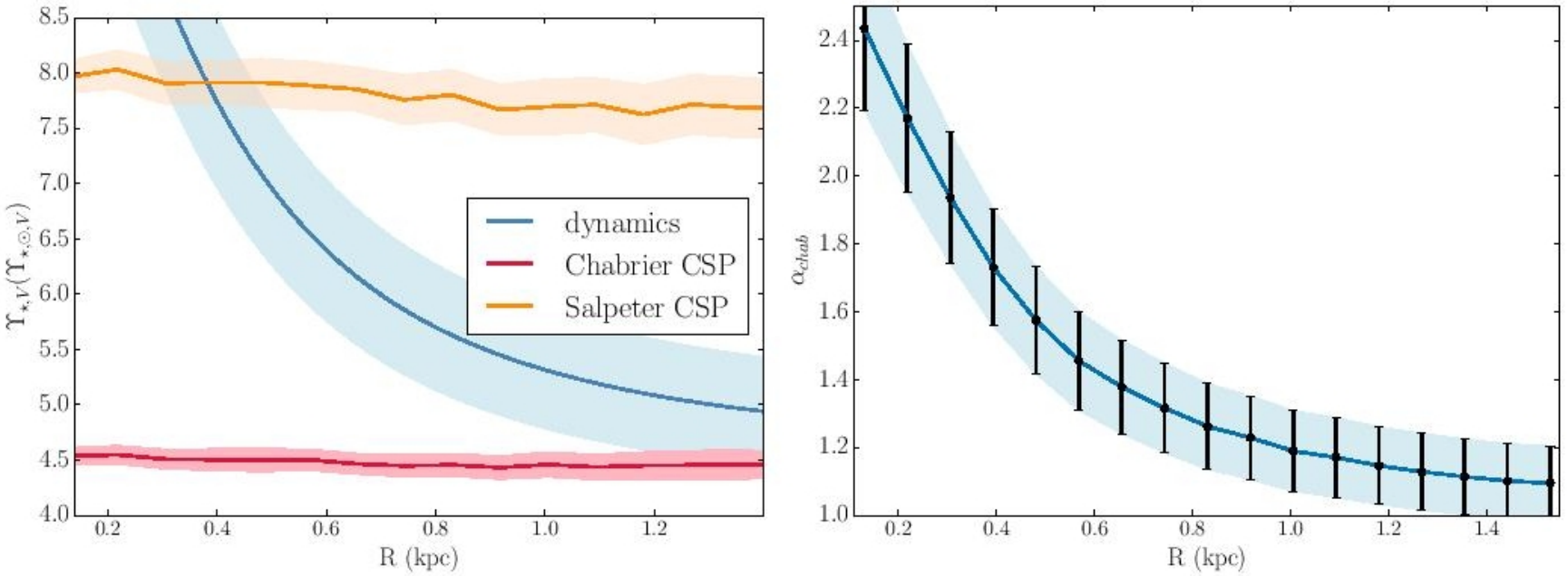

Figure 4. Left: The stellar mass-to-light ratio inferred dynamically, shown in blue, declines much more rapidly than can be achieved by gradients in the age, metallicity, star formation history and dust extinction of the stellar populations under a fixed IMF, suggesting that an IMF gradient may be the driving factor. Indeed, the stellar mass-to-light ratio is consistent with stellar population models that assume a Salpeter IMF at small radii, but consistent with stellar population models assuming a Chabrier-like IMF at larger radii. Right: the IMF mismatch-parameter α_{chab} as defined in Equation 15, again showing that the mismatch between the dynamically-inferred stellar mass-to-light ratio and the stellar population-modelling-inferred stellar mass-to-light ratio under the assumption of a Chabrier

Во внешних областях – IMF Chabrier, в центре – bottom-heavy

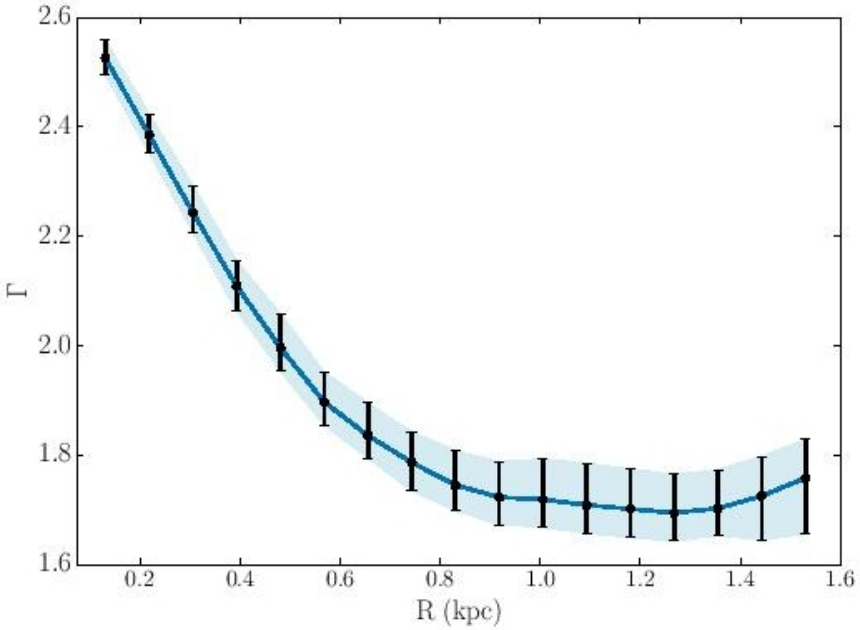

Figure 5. Inference on the slope of a broken-power-law IMF with slope $\xi = 2.3$ for $M > 1M_{\odot}$ and $\xi = \Gamma$ for $M < 1M_{\odot}$. We use FSPS to calculate magnitudes on a grid of ages, metallicities and Γ, and obtain the posteriors on these quantities based on 11-band HST photometry and our dynamical inference on the projected stellar mass as a function of radius. Our model clearly requires an IMF that becomes increasingly bottom-heavy towards the centre. Nevertheless, it is possible that alternative models which allow greater flexibility in other stellar population properties may also be able to reproduce the photometry and mass inference simultaneously.